Received: 15 September 2022 | Revised: 24 December 2022 | Accepted: 12 January 2023

DOI: 10.1002/cta.3560

ORIGINAL PAPER

WILEY

Intelligent wide-area damping controller for static var compensator considering communication delays

Faisal Jamsheed | **Sheikh Javed Iqbal**

Department of Electrical Engineering, National Institute of Technology Srinagar, Hazratbal, Srinagar, Jammu and Kashmir, 190006, India

Correspondence
Faisal Jamsheed, Department of Electrical Engineering, National Institute of Technology Srinagar, Jammu and Kashmir, India.
Email: faisaljamsheed@nitsri.ac.in

Present address
Faisal Jamsheed, Department of Electrical Engineering, National Institute of Technology Srinagar, Jammu and Kashmir, India.

Summary

This paper utilizes a static var compensator in coordination with an intelligent online controller, to enhance the oscillation damping of the power system at various operating conditions and communication delays. For system identification, a linear identifier is used that ensures a low computational burden and facilitates its real-time implementation. This identifier accurately estimates the system's local linear model using local measurements and continuously updates its parameters in real time to account for system's changing operational states. The learning rate of the identifier is also adaptively adjusted such that the stability of the learning algorithm and optimal speed of convergence are guaranteed. The location of the controller is selected based upon the controllability and bus voltage participation factors, and an effective feedback signal is obtained using the observability. An empirical expression has also been proposed to offset the effects of communication time delays caused due to use of wide-area signals. Time-domain simulations are performed on single- and multi-machine power systems to check the efficacy of the proposed intelligent controller. The performance of the controller is compared with the residue-based conventional controller and also with the recently proposed wide-area damping controller.

KEYWORDS

adaptive control, low-frequency oscillations, neural network, static var compensator, wide-area damping control

1 | INTRODUCTION

Exponential increase in domestic and industrial loads with disproportionate expansion of the power system has led the utilities to operate the power system with reduced stability margins. As a result, the stability of the power system is very much dependent on a particular operating state. Disturbances like load changes or faults can trigger low-frequency oscillations (LFOs) (0.2 to 2 Hz), and these occur due to energy transfer between speed variations of the rotor and the generated electrical power.[1] The damping of these oscillations is a prerequisite for the secure and reliable functioning of the power system. Conventionally, power system stabilizer (PSS) has been used to mitigate LFOs in the power system.[2] However, its adverse effect on the system's voltage profile and its effectiveness in damping local modes have constrained its application as an initial measure to improve system's dynamic stability.[3] Therefore, it is essential to employ alternative techniques in the power system that enhance its oscillation damping and simultaneously stabilizes its voltage profile.

One way of addressing this issue is by adding adequate reactive power to the system during the occurrence of a disturbance. The addition of reactive power for some cycles following a disturbance can help the power system regain its stable condition, and with proper control, improved oscillation damping and simultaneous stabilization of the voltage profile can be achieved. Among various var generating devices, the static variable compensator (SVC) is generally preferred flexible-ac-transmission-system (FACTS) device due to its quick response.[4]

SVC has mostly been utilized for voltage regulation by directly controlling the reactive power flow at weak points in the system, power-factor corrections, and reduction in power losses.[5] It has also been utilized to increase the damping of low-frequency electromechanical oscillations in the power system by adding an additional control to its voltage regulation controller. The output of this additional controller is generally obtained using conventional lead-lag and proportional-integral-derivative controllers.[6–11] In Hasanvand et al,[6] the parameters are selected so that the eigenvalues corresponding to the critical oscillatory mode are shifted to a stable region, which is determined using interval-polynomial control methodology and Kharitonov's theorem. In Al-Alawi and Ellithy,[7] artificial neural networks have been used to optimize the parameters of the proportional-integral controller for enhancing the damping in the system. In some studies, optimization techniques are utilized to find the parameters of the lead-lag supplementary controller, which include genetic-algorithm-based optimization,[8] a meta-heuristic-bat algorithm,[9] ant colony optimization,[10] and firefly algorithm.[11] Advanced controllers like model predictive controller (MPC) have also been used with the SVCs to damp the low-frequency oscillations in the power systems. In Kassem and Abdelaziz,[12] SVC is connected at terminal bus to stabilize load voltage through compensation of reactive power using an exponentially weighted functional MPC (FMPC), which puts less calculation effort as compared with conventional MPC with large prediction horizon. The improved wide-area damping controllers (WADCs) and the deterioration of the controller performance due to communication delays have also been reported.[11,13–15] The effects of these delays have been compensated using methods like Pade-approximation compensation[14] and unified Smith predictor compensation,[15] and so forth.

The aforementioned control schemes have constant parameters and cannot be adaptively modified with the system's varying operating states. Continual redistribution in generation and load demand, system faults and outages, and continuous structural augmentation lead to frequent changes in the operation of the power system. Controller parameters that perform well for a particular set of operating conditions may be ineffective for some other condition. As a result, conventional controllers are designed with a trade-off between the values achieved for the light, nominal, and overloaded scenarios. Therefore, adaptive control schemes are required that work adequately in varying power system scenarios.

Adaptive control strategies for the design of supplementary SVC controllers have also been reported, which include fuzzy-logic-based control[16] and fuzzy-sliding-mode control scheme.[17] A multi-objective MPC is applied with the SVC for power oscillation damping.[18] To make the control scheme adaptive, a time-varying weight is added to the objective function so the controller tracks the varying dynamics of the system. In Lu et al,[19] controller parameters were optimized using ant-colony optimization at nominal operating conditions, and fuzzy-based control was utilized during off-nominal conditions. Various neural network-based control schemes have been reported to enhance oscillation damping of the power system through SVC.[20–22] Other neuro-based control scheme used for such application include neuro-fuzzy-based control.[23,24] However, the above-discussed controllers lack some essential features required for their practical realizability, like online adjustments and simple structure. These control structures utilize multiple nonlinear neurons, which substantially increases the floating-point operations and reduces the speed of identification with practically limited processing resources and consequently affects the controller performance. Moreover, some adaptive techniques also lack assurance of the stability. With these limitations, power system industry still prefers conventional controllers, and the above-discussed intelligent adaptive methodologies have in general not been able to find practical applications.

In this study, an improved neural network-based adaptive control scheme is presented that aims to overcome the limitations in the aforementioned controllers. It comprises a simple, linear neural identifier whose parameters are adjusted in accordance with the system's operating conditions. The learning rate of the identifier adaptively adjusts itself such that the learning algorithm's convergence and optimal speed of convergence are guaranteed. The controller, whose parameters are dependent on the identifier parameters, provides optimal and swift control action. The developed controller was implemented in the MATLAB/Simulink environment and applied to a benchmark single-machine infinite-bus system and a two-area four-machine system. When compared with highly complex neural network structures used in previous studies, the proposed control scheme provides rapid system identification and outstanding control performance. Moreover, the performance was validated under varied operating conditions and time delays.

The rest of the paper is organized into the following sections: Section 2 describes the configuration and design of the SVC for the oscillation damping applications. The description of the time delays and the method to compensate its effects are presented in Section 3. Section 4 gives the detailed model of the proposed intelligent control scheme. The performance evaluation is given in Section 5 followed by the conclusions of the study presented in Section 6.

2 | STATIC VAR COMPENSATOR

SVC is a variable-reactance device that is used to control the reactive power flow in a power system. Moreover, this device can also indirectly alter the active power flow in the system through the alteration of impedance, voltage, and phase angle. With proper control, it can, therefore, be used to counter the changes in active and reactive power balance caused by the disturbances. SVC is presently used in many power networks across the globe, and there are as many as 1500 SVCs with a total capacity of 100 Gvar installed for different applications.[4] The circuit diagram of the SVC used in this study is shown in Figure 1.

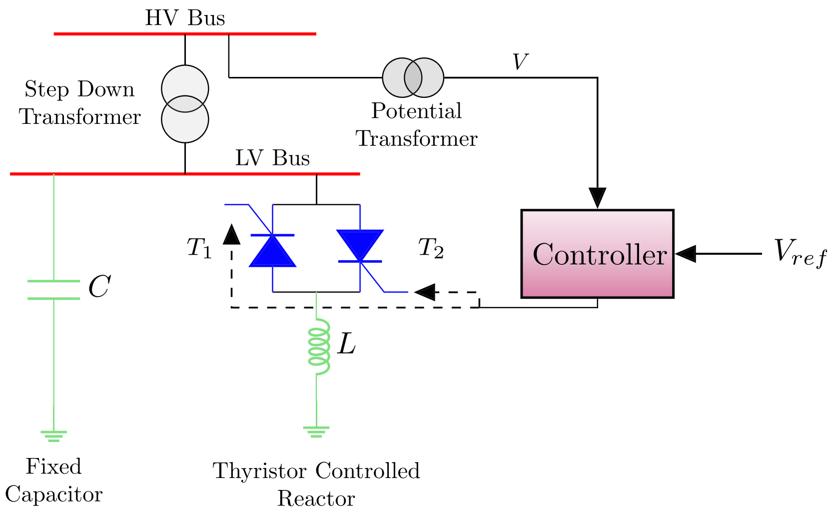

FIGURE 1 Fixed-capacitor thyristor-controlled SVC. [Colour figure can be viewed at wileyonlinelibrary.com]

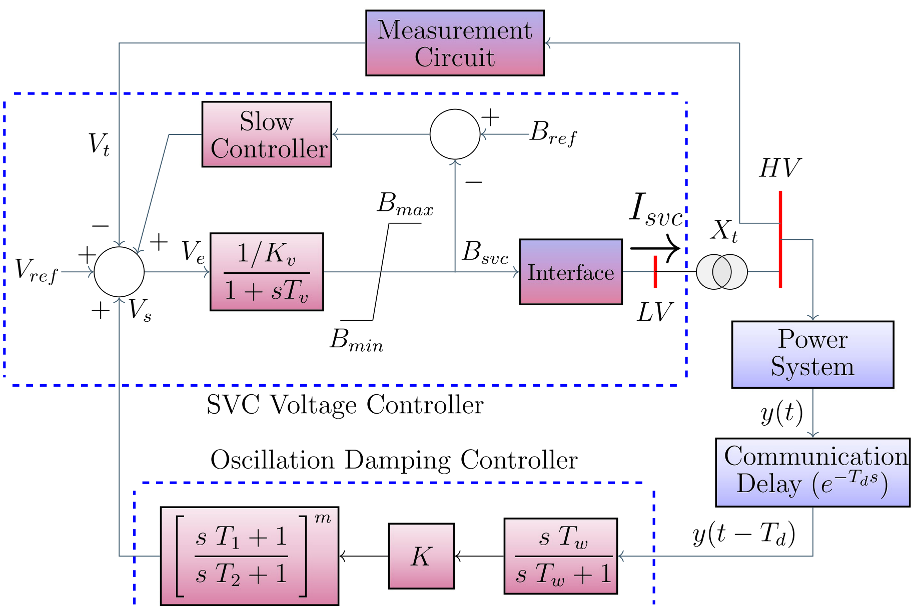

FIGURE 2 Control scheme of the SVC. [Colour figure can be viewed at wileyonlinelibrary.com]

2.1 | Control structure of the static var compensator

Design of the control scheme for SVC is dependent on its application, that is, voltage regulation, power transfer enhancement, or oscillation damping. SVC's voltage controller does not add any oscillation damping; however, with proper SVC placement and a suitable feedback signal, a supplementary control scheme can provide sufficient oscillation damping together with a stable voltage profile.[14] As shown in Figure 2, the first-order voltage controller is used to provide voltage stabilization, which includes a droop (K_v) and a time constant (T_v) to account for the delays caused by the TCR firing circuits and measurement circuits. To provide oscillation damping, a supplementary control signal V_s is added to the voltage-error signal V_e, as shown in Figure 2. To keep the SVC at its nominal condition after the disturbance is tackled, a slow controller is also added so as not to interfere with the other system controllers. Moreover, the feedback signal of the controller and the location of SVC placement should be sensitive to the oscillation mode of interest. As a result, observability and controllability corresponding to the oscillation modes of interest are the logical choices for their selection.

2.2 | Modal analysis

System's small-signal model can be represented by the following equations:

$$\Delta\dot{\boldsymbol{x}} = \boldsymbol{A}\Delta\boldsymbol{x} + \boldsymbol{B}\Delta u \tag{1}$$

$$\Delta y = \boldsymbol{C}\Delta\boldsymbol{x} \tag{2}$$

where $\boldsymbol{A}, \boldsymbol{B}$, and $\boldsymbol{C}$ are the state transition, input and output matrices, respectively. The transfer function corresponding to the linearized system is given by

$$G(s) = \sum_{i=0}^{n} \frac{\boldsymbol{R}_i}{s - \lambda_i} \tag{3}$$

where $\boldsymbol{R}_i$ is the residue matrix corresponding to the eigenvalue λ_i and is given by[14]

$$\boldsymbol{R}_i = \boldsymbol{C}\,\boldsymbol{v}_i\,\boldsymbol{w}_i^T\boldsymbol{B} \tag{4}$$

where $\boldsymbol{v}_i$ and $\boldsymbol{w}_i$ are the right and left eigenvectors corresponding to the eigenvalue λ_i. The residue value for the input p and output l is given by

$$R_i^{lp} = \boldsymbol{C}_l\,\boldsymbol{v}_i\,\boldsymbol{w}_i^T\boldsymbol{B}_p. \tag{5}$$

Residue matrix can also be represented as

$$\boldsymbol{R}_i = \boldsymbol{O}_{\boldsymbol{b}i} \times \boldsymbol{C}_{\boldsymbol{t}i} \tag{6}$$

where $\boldsymbol{O}_{\boldsymbol{b}i}$ is observability matrix that determines ability to ascertain system states by observing its output and is given by

$$\boldsymbol{O}_{\boldsymbol{b}i} = \boldsymbol{C}\,\boldsymbol{v}_i \tag{7}$$

and $\boldsymbol{C}_{\boldsymbol{t}i}$ is controllability matrix and refers to a system's ability to reach to its desired state in a finite time duration when a controlled input is applied it. Controllability matrix is given by

$$\boldsymbol{C_{ti}} = \boldsymbol{w}_i^T \boldsymbol{B}. \tag{8}$$

Higher the controllability, lesser is the control effort for damping the oscillation mode. However, voltage profile should not be deteriorated while enhancing the oscillation damping. Therefore, the method proposed in Zhang et al[25] provides an effective way to solve this problem. Bus voltage participation factor (BVPF) gives the extent of voltage instability at a particular bus and is represented by $P_{J_{ji}}$, that is, participation factor of bus j corresponding to the mode i and computed using

$$P_{J_{ji}} = \boldsymbol{v_{Jji}} \boldsymbol{w_{Jij}}. \tag{9}$$

v_J and w_J are the right and left eigenvectors corresponding to the minimum eigenvalue of the reduced Jacobian matrix J_R. The relationship of these eigenvectors and reduced Jacobian matrix is given by

$$J_R = \boldsymbol{v_J} \lambda_J \boldsymbol{w_J} \tag{10}$$

where λ_J is the diagonal matrix of eigenvalues corresponding to matrix J_R. J_R is calculated by neglecting the changes in power due to change in the voltage while solving power-flow equations using Newton-Raphson method[25] and is represented as

$$\Delta V = J_R^{-1} \Delta Q. \tag{11}$$

Solving (11) using (10) and (9) yields

$$\Delta V = \sum_i \frac{P_{J_{ji}}}{\lambda_{J_i}} \Delta Q \tag{12}$$

which implies change in voltage will be rapid with a small change in reactive power if the magnitude of eigenvalue is small. The extent of voltage instability at a particular bus will, therefore, be determined by the participation factor for the lowest eigenvalue of the matrix J_R. Selection of SVC location, based upon controllability and BVPF, will provide a balanced control effort to damp the oscillation as well as maintaining the voltage profile of the power system.

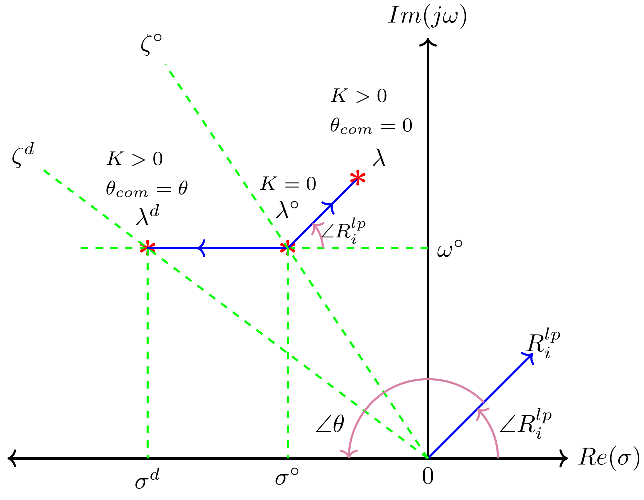

FIGURE 3 Eigenvalue shift by residue-based controller. [Colour figure can be viewed at wileyonlinelibrary.com]

2.3 | Residue-based damping controller

The residue angle ($\angle R_i^{lp}$), as shown in Figure 3, gives the displacement direction of the eigenvalue in the s-plane.[13,14] This direction can be reoriented toward left using the lead-lag compensation, and compensation angle (Figure 4) is calculated using

$$\phi_{com} = \pi - \angle R_i, \quad 0 < \angle R_i < \pi \tag{13}$$

with positive feedback,[13,14] and

$$\phi_{com} = -\angle R_i, \qquad -\pi < \angle R_i < 0 \tag{14}$$

with negative feedback.[26] The required compensation (ϕ_{com}) is provided by multistage (n_s) lead-lag transfer function given by

$$H_{com}(s) = \left[\frac{1 + sT_1}{1 + sT_2}\right]^{n_s} \tag{15}$$

A single stage is able to provide phase compensation of $\pi/3$ radians, and T_1, T_2 are calculated using the following equations

$$\frac{T_2}{T_1} = \frac{1 - sin\left(\frac{\phi_{com}}{n_s}\right)}{1 + sin\left(\frac{\phi_{com}}{n_s}\right)} \tag{16}$$

$$T_1 T_2 = \frac{1}{\omega_f^2} \tag{17}$$

where $\omega_f \rightarrow$ mode frequency. The displacement of the eigenvalue in the s-plane due to $H_{com}(s)$ is given by

$$\Delta\lambda_i = |R_i^{lk}| \times |H_{com}(\lambda_i)| \tag{18}$$

and, to place the eigenvalue (initially at λ°) at the desired place λ^d, an additional gain K is added with lead-lag compensator and the value of K is selected using the root-locus plots.

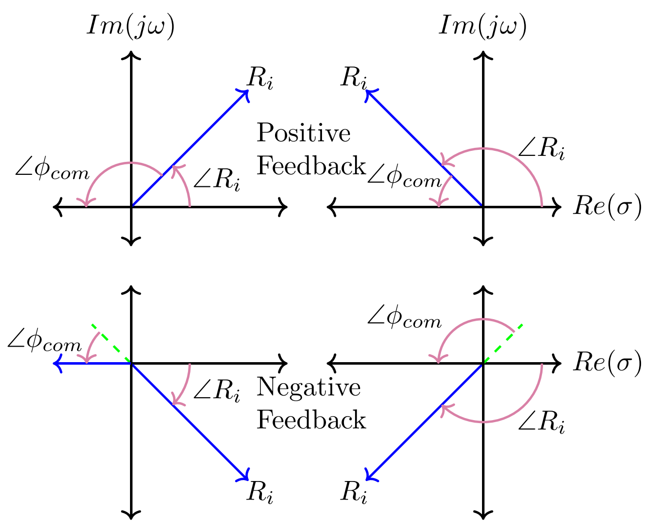

FIGURE 4 Compensation by residue-based controller. [Colour figure can be viewed at wileyonlinelibrary.com]

3 | COMMUNICATION DELAY

With the development of wide-area measurement systems (WAMSs) and their integration with phasor measurement units (PMUs), phasor data concentrators (PDCs), and communication systems, remote signals can be transmitted to the control centers digitally once or twice every fundamental cycle depending upon the refresh rate of PMUs.[27,28] As a result, widely dispersed signals can be centralized in the control center and sent to different locations across the power network, and hence, WADC can be utilized as a real-time alternative to the decentralized control. PMUs provide access to wide-area measurements in the power system, and the signals are transmitted to the controller with the help of PDCs. PMUs also facilitate time-synchronization of multiple wide-area signals through global positioning system (GPS) clock.[29]

An important aspect to consider while designing WADC is the delay time in the communication system. The delay time typically varies from a few to hundreds of milliseconds and is dependent on the transmission protocols and type of communication lines used. It is also dependent upon the distance between the measuring equipment and the position of the SVC controller.[29] Mathematically, the delay can be represented by the following equation:

$$D_l(s) = e^{-T_d s} \tag{19}$$

where T_d is the time delay. It can be observed that (19) is not a rational function. However, to realize (19) in finite dimensions, methods like Pade approximation, hyperbolic function, Laguerre polynomial, or Bessel function are used.[14] Among these, the Pade approximation is found to be the most accurate representation of the delay and is given by[30]

$$P_d(s) = \frac{\sum_{i=0}^{g} \frac{(g+h-i)!g!(-sT_d)^j}{i!(g-i)!}}{\sum_{i=0}^{h} \frac{(g+h-i)!r!(sT_d)^j}{i!(h-i)!}} \tag{20}$$

where g and h represent the order of the Pade approximation. If $g = h = n_p$, (20) can be expanded and represented as

$$P(s) = \frac{1 - p_1 s + p_2 s^2 - \ddots \pm p_n s_p^n}{1 + p_1 s + p_2 s^2 + \ddots \pm p_n s_p^n} \tag{21}$$

where n_p is the order of Pade approximation and $p_1, p_2, \ldots, p_n$ are its coefficients. Second-order Pade approximation, with a degree of numerator lower than denominator, is observed to sufficiently represent delay, as shown in Figure 5, and is given as

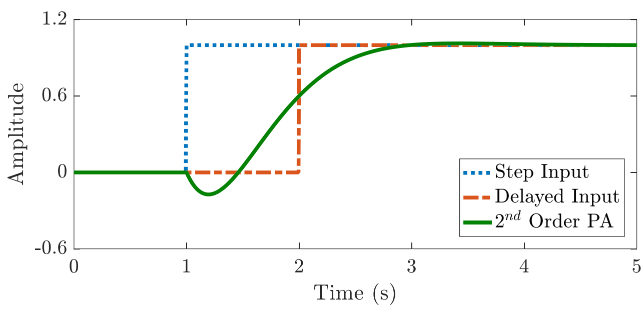

FIGURE 5 Step response of the Pade approximation (PA) of second order $((g,h) = (1,2))$. [Colour figure can be viewed at wileyonlinelibrary.com]

$$G_d(s) = \frac{-2T_d s + 6}{T_d^2 s^2 + 4T_d s + 6}. \tag{22}$$

The delay causes a phase lag in the feedback signal, and this lag depends upon the delay time and the frequency of oscillation. The lag in the feedback signal causes deterioration in the controller performance as the controller is usually designed without considering the delay.[14] Various methods have been reported for compensating the phase lag.[14] However, either these methods have applications within a specific range of time delays or they are based on various approximations, which do not apply to a wide range of time delays. In this study, lead-lag-based phase compensation is proposed, whose parameters are dependent on the delay time. These time constants are determined using an empirical expression, which is derived through the simulation experiments. The transfer function representing this compensation is given by

$$G_{dc}(s) = \left[\frac{1 + sT_{dc_1}}{1 + sT_{dc_2}}\right]^3 \tag{23}$$

$$T_{dc_1} = \frac{17}{40} \times T_d \tag{24}$$

$$T_{dc_2} = 0.01. \tag{25}$$

Figure 6 shows the plots of the delay phase ($\angle G_d(s)$), delay phase compensator (DPC) ($\angle G_{dc}(s)$), and net phase ($\angle G_d(s) + \angle G_{dc}(s)$) for few time delays. It can be observed from the plots that net phase is nearly 0 in the frequency range of interest, indicating good phase compensation of delay can be achieved for the practical time delay range.

4 | LINEAR-NEURO-ADAPTIVE CONTROLLER

The operating conditions in the power system change frequently, and hence, the performance of the residue-based damping controller might not always be satisfactory. Moreover, characteristics of various power system parameters are nonlinear and may pose additional difficulties. Online system identification-based control scheme is therefore required,

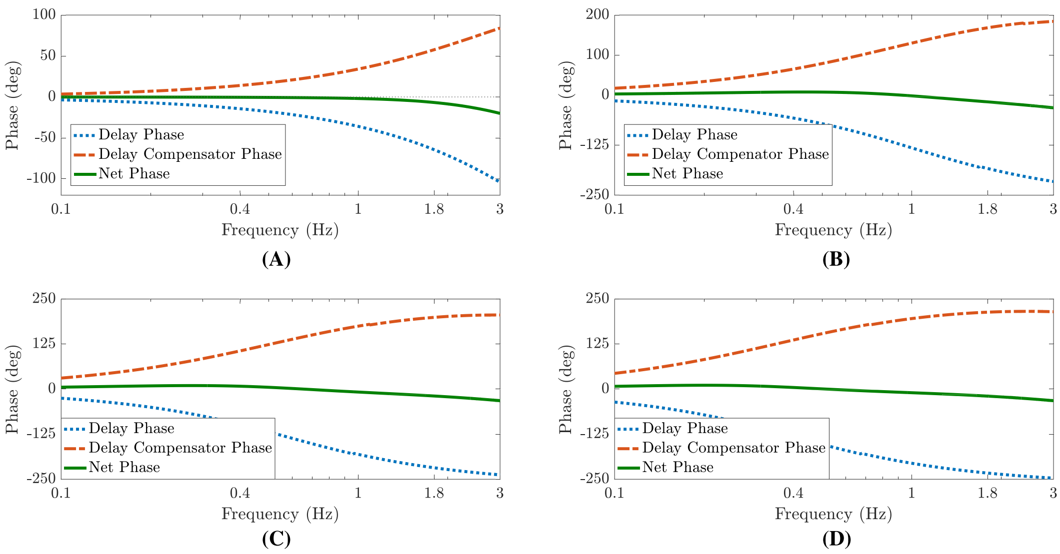

FIGURE 6 Phase of the delay and DPC for (A) 0.1 s, (B) 0.4 s, (C) 0.7 s, and (D) 1 s. [Colour figure can be viewed at wileyonlinelibrary.com]

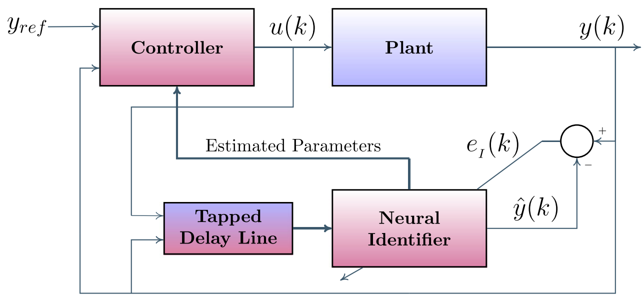

FIGURE 7 Functional block diagram of the LNAC scheme. [Colour figure can be viewed at wileyonlinelibrary.com]

which assesses the system's changing dynamic scenarios and accordingly modifies the control signal in real time (online). Since dynamic inputs and outputs can be easily mapped using the neural network, which has led to the development of various neural network-based adaptive control schemes.[31–34] These controllers have also been applied with the SVC for oscillation damping application and have been found to overperform the conventional controllers.[20–24]

In this study, a linear-neuro-adaptive controller (LNAC) is presented to provide enhanced oscillation damping under varied operating scenarios. As shown in Figure 7, the LNAC consists of the system identification and controller. The system identifier approximates the dynamics of the plant by adjusting its parameters (weights) online, and its prominent feature is its architecturally minimal structure, comprising a single linear neuron. When compared with the existing neural architectures in the literature, the connection weights are relatively small in number. The control law is framed such that the parameters of the controller are coupled to the estimated parameters of the identifier and, at each sample period, an appropriate signal is generated from the controller such that the output of the plant follows the reference.

4.1 | Neural identifier

The plant output can be expressed as a function of the previous input (m) and output samples (n) as follows:

$$y(k) = f(\boldsymbol{I}(k-1)) \tag{26}$$

$$\begin{aligned}\boldsymbol{I}(k-1) = [&u(k-1), u(k-2), u(k-3), \ \ldots\ldots, \ \ u(k-m-1), u(k-m),\\ &y(k-1), y(k-2), y(k-3), \ \ldots\ldots, \ \ y(k-n-1), y(k-n)].\end{aligned} \tag{27}$$

The neural network autoregressive with exogenous input (NNARX) model can be used to approximate the relationship between input and output expressed as[35]

$$\hat{y}(k) = f'(\boldsymbol{I}(k-1), \boldsymbol{W}^I(k-1)) \tag{28}$$

$$\boldsymbol{W}^I(k) = [w_1^I(k), w_2^I(k), \ \ldots., \ w_{m+n}^I(k)] \tag{29}$$

where $w_i{}^I$ is the weight attached to the inputs of the neural identifier. A single neuron having linear activation function, as shown in Figure 8, can therefore be represented as

$$\hat{y}(k) = \boldsymbol{I}(k-1)\boldsymbol{W}_I^T(k-1). \tag{30}$$

The error between the output of plant and that of the identifier is represented by

$$e_I(k) = y(k) - \hat{y}(k). \tag{31}$$

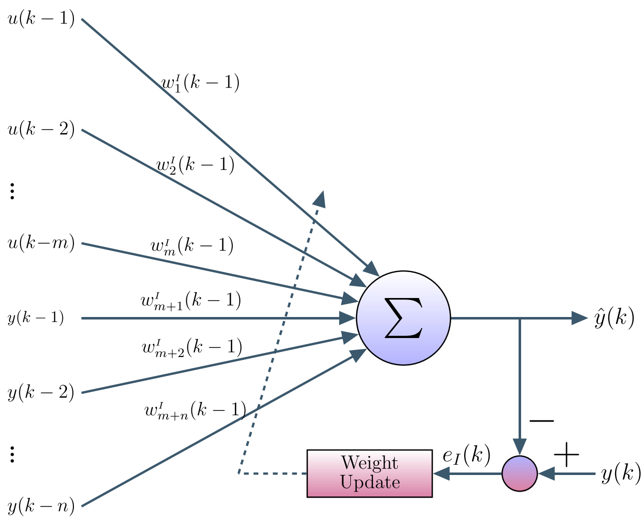

FIGURE 8 Neural identifier. [Colour figure can be viewed at wileyonlinelibrary.com]

The neural identifier's weights are modified through the back-propagation method such that, after a few iterations, identifier output $\hat{y}(k)$ approaches plant output $y(k)$ using the cost function C_I for the identification system defined by

$$C_I(k) = \frac{1}{2}[e_I(k)]^2. \tag{32}$$

With learning rate η, the gradient descent algorithm is employed to update the parameters (weights) of the identifier through the following recursive equation:

$$\boldsymbol{W}^I(k) = \boldsymbol{W}^I(k-1) + \eta\left[-\frac{\partial C_I(k)}{\partial \boldsymbol{W}^I(k-1)}\right]. \tag{33}$$

Using (30) to (32) to solve (33), results in $\boldsymbol{W}^I(k)$ to be represented in the form as

$$\boldsymbol{W}^I(k) = \boldsymbol{W}^I(k-1) + \eta e_I(k)\boldsymbol{I}(k-1). \tag{34}$$

The accurate identification of the plant is achieved by the convergence of (34), which corresponds to $e(k) \to 0$. The identifier then feeds the plant information (captured in weights) to the controller, enabling the plant to produce the desired output.

4.2 | Controller

The goal of a controller is to minimize the mismatch between the observed and anticipated plant output represented by

$$e_c(k+1) = y_{ref}(k) - \hat{y}(k+1). \tag{35}$$

In order to obtain optimum control action, control error $e_c(k+1)$ must be decreased, and moreover, the control action must be constrained to practically realizable values. Therefore, the cost function $Cc(k)$ for the controller is proposed, which reduces control error while restricting the controller output from generating unacceptable high values. The cost function is expressed by

$$C_c'(k) = \frac{1}{2}[y_{ref}(k) - \hat{y}(k+1)]^2 + \frac{1}{2}\alpha[u(k) - \beta u(k-1)]^2. \tag{36}$$

The proportionate penalty weightage on the control signal and change in the control signal is determined by β with $\alpha > 0$. While $\beta = 0$ and $\alpha > 0$ solely penalizes the $u(k), \beta = 1$ and $\alpha > 0$ penalizes the change in control action. The plant output derivative is added to (36) to offset the drop in transient performance that these penalties often induce in the controller. The revised control law is thus stated as

$$C_c(k) = \frac{1}{2}\left[\left[y_{ref}(k) - \hat{y}(k+1)\right]^2 + \gamma\left[y(k+1) - y(k)\right]^2 + \alpha\left[u(k) - \beta u(k-1)\right]^2\right] \tag{37}$$

where γ determines the weightage given to the derivative term in the control law. The cost function defined for the controller C_c is minimized with respect to the controller output $u(k)$ by setting

$$\frac{\partial C_c(k)}{\partial u(k)} = 0 \tag{38}$$

Solving (38) using (30) yields

$$\begin{aligned} u(k) \; = & -\frac{\alpha + (1+\gamma)[w^I_{n+1}]^2}{w^I_{n+1}}\Big[(1+\gamma)\boldsymbol{I}^I(k)\boldsymbol{A}[\boldsymbol{W}^I(k-1)]^T \\ & + \frac{\alpha\beta}{w^I_{n+1}} u(k-1) + \gamma y(k) - y_{ref}(k)\Big] \end{aligned} \tag{39}$$

where I is the identity matrix and $\boldsymbol{A}$ is given by

$$\boldsymbol{A} = \begin{bmatrix} 0 & 0 & 0 & \dots & 0 \\ 0 & 1 & 0 & \dots & 0 \\ 0 & 0 & 1 & \dots & 0 \\ \vdots & \vdots & \vdots & \dots \vdots & \vdots \\ 0 & 0 & 0 & \dots & 1 \end{bmatrix}_{(m+n)}$$

4.3 | Stability analysis

The learning algorithm's stability and the speed of convergence described by (34) rely upon the appropriate learning rate. Small value of the learning rate guarantee convergence, but the learning becomes sluggish, and its large value may produce oscillations and result in divergence. Furthermore, assigning a constant value to the learning rate does not promise reliable performance under all operational environments. Henceforth, the value of the learning rate must be adaptively modified at each sampling instant to ensure stability as well as appropriate convergence speed. Therefore, an adaptive learning rate ($\eta(k)$) is obtained using the *second method of Lyapunov* that assures algorithm stability as well as optimum convergence speed.

Theorem 1. *The weights update algorithm in (34) will converge and the identifier output will follow the plant output if the learning rate $\eta(k)$ satisfies the following criteria*

$$\eta(k) = \frac{\eta_o}{\|\boldsymbol{I}(k-1)\|_2^2} \tag{40}$$

where $0 < \eta_o < 2$ and $\|(.)\|_2$ represents the Euclidean norm.

Proof. Appendix A. ■

Other key approaches for assuring system stability are system passivity and dissipativity.[36] In Appendix B, passive and dissipative system definitions are provided.

Theorem 2. *The weight vector of the LNAC* ($\boldsymbol{W}^{I}(k)$) *will approach its ideal value* $\boldsymbol{W}^{o}$ *and the mapping of* $\Delta\boldsymbol{W}^{I}(k) \rightarrow \boldsymbol{W_e}(k)$ *will be passive and dissipative* $\Leftrightarrow$ $\eta(k)$ *of the identifier fulfills (40).*

Proof. Appendix C. ■

It is consequently established that if $\eta(k)$ is continuously updated according to (40), $\boldsymbol{W}^{I}(\mathrm{k}) \rightarrow \boldsymbol{W}^{o}$.

4.4 | Implementation of the linear-neuro-adaptive controller

The sample time of the LNAC was taken as 0.025 s and the lag space (m, n) was taken as 3.[20,35] These values reduce the computational burden of the control scheme along with the satisfactory identification of the power system. The constant of the LNAC η_o was optimally taken as 1 and the other constant ϵ as 0.001. In the LNAC, mainly following two operations are executed at each sample time step:

1. The weights (parameters) of the identifier are adjusted to minimize the identification error.
2. These parameters are communicated to the optimal controller, that provides adequate control action.

Figure 9 depicts the full methodology for implementing the LNAC algorithm.

5 | DYNAMIC SIMULATION RESULTS

In order to assess and evaluate the effectiveness of the residue-based damping controller (RBDC) and LNAC for damping LFOs, simulation tests were conducted on a single-machine infinite-bus system and an interconnected two-area four-machine system.

5.1 | Single-machine infinite-bus power system

The single-machine infinite-bus (SMIB) power system is shown in Figure 10. It comprises a synchronous generator simulated by a seventh-order nonlinear model with a rating of 160 MVA and an infinite bus which is connected to synchronous generator via a transmission line.[37] The synchronous generator is equipped with IEEE-type-1S static excitation system.[37] The parameters and rating of the SVC (Base = 160 MVA) used with the SMIB power system are given in Table 1.

5.1.1 | Modal analysis

For modal analysis, the SMIB system is linearized around the nominal operating condition ($P_G = 0.975$, $Q_G = 0.12$, base power = 160 MVA). A low-frequency oscillation mode ($-0.36 \pm j10.2$) is observed in the system with a frequency of 1.62 Hz and a low damping ratio (ζ) of 0.036. For selection of an effective SVC location, modal controllability and BVPF were calculated using (8) and (9), respectively. The controllability order corresponding to the oscillation mode and the BVPF order corresponding to the lowest eigenvalue of J_R (1.64) are given in Table 2. It is evident that the controllability and BVPF order both favor the SVC's installation on bus 1. The effective feedback signal was selected by calculating the observability of various power system signals and is given in Table 3. As shown in Table 3, the speed deviation of the generator $\Delta\omega$ having the best observability is selected as the SVC controller's feedback signal.

5.1.2 | Comparison between RBDC and LNAC

The time constants of RBDC are calculated by solving (13) to (17) using (5) for the poorly-damped local mode. The values of the $\angle \mathrm{R}_{\mathrm{i}}^{\mathrm{lp}}$ and n_s are -127.7° and 3, respectively, and the values of T_1 and T_2 are obtained as 0.22 and 0.043,

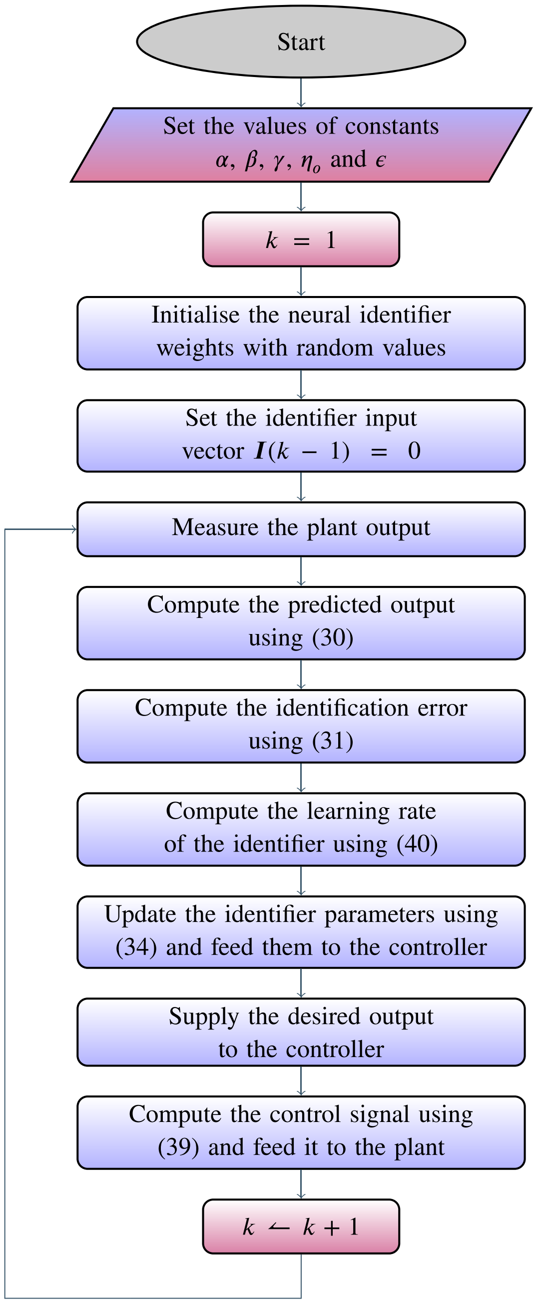

FIGURE 9 Algorithm for implementation of the proposed LNAC scheme. [Colour figure can be viewed at wileyonlinelibrary.com]

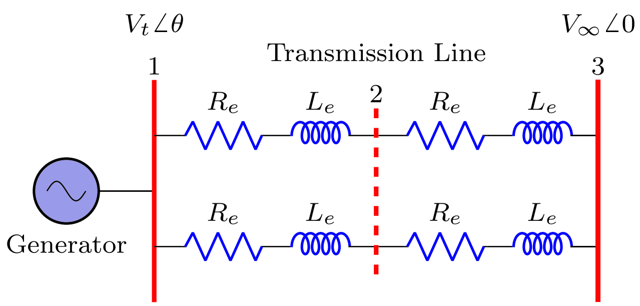

FIGURE 10 Configuration of single-machine infinite-bus system. [Colour figure can be viewed at wileyonlinelibrary.com]

TABLE 1 SVC parameters.

B_{ref}	0.025	T_v	0.15
B_{min}	−0.075	K_v	0.02
B_{max}	0.1	$V_{s_{min}}$	−0.1
X_t	0.08	$V_{s_{max}}$	0.1

TABLE 2 C_t and BVPF.

	Bus number	
S.No	**C_t rank**	**BVPF rank**
1.	1	1
2.	2	2
3.	3	-

TABLE 3 Observability.

S.No.	Signal O_b rank	S.No.	Signal O_b rank
1.	$\Delta\omega$	4.	P_2
2.	$\Delta\delta$	5.	P_3
3.	P_1	6.	Q_3

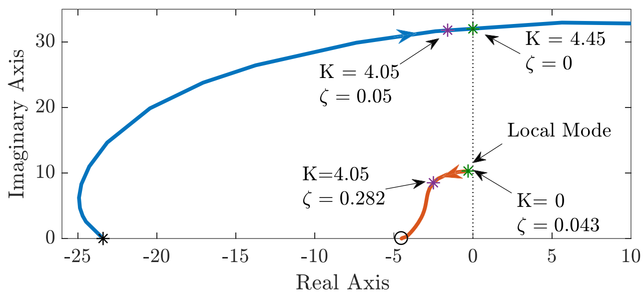

FIGURE 11 Root-locus plot for SMIB system for loading condition I. [Colour figure can be viewed at wileyonlinelibrary.com]

respectively. The gain of the controller is selected using the root-locus technique as shown in Figure 11. It is observed that with the increase in the value of K, the damping of the local mode is increased. However, there is another mode (due to SVC) in the system whose damping decreases as the gain is increased. At $K = 4.45$, it is observed that this mode crosses the imaginary axis. With the damping ratio of this mode set at 0.05, the value of K thus obtained is 4.05 and at this value, the ζ of local mode is 0.282.

For LNAC, $u(k) = V_s$, $y(k) = \Delta\omega$ and $y_{ref} = 0$ (Figures 2 and 7). The penalty factors for the nominal operating condition were adjusted as $\alpha = 1$, $\beta = 0$, $\gamma = 0$, respectively. Once adjusted, these value are kept fixed for a particular power system. The tracking performance of the proposed linear neural identifier is verified since the controller output is dependent on the exact system identification. To check the tracking capabilities of the proposed identifier, a 10 % pulse disturbance is given to the V_{ref} of the SVC with $V_s = 0$. The plots of the actual speed deviation of the machine $\Delta\omega$ and that of the identifier output are shown in Figure 12. From the plot in Figure 12A, a mismatch in the beginning portion is observed, which is due to the random initialization of the weights, called as learning transient. However, this mismatch reduces quickly in the same iteration for the subsequent oscillations. The identifier output and actual rotor-speed output are observed to be very close in the second iteration (Figure 12B). The error is observed to reduce quickly, indicating the fast learning capability of the linear neural identifier.

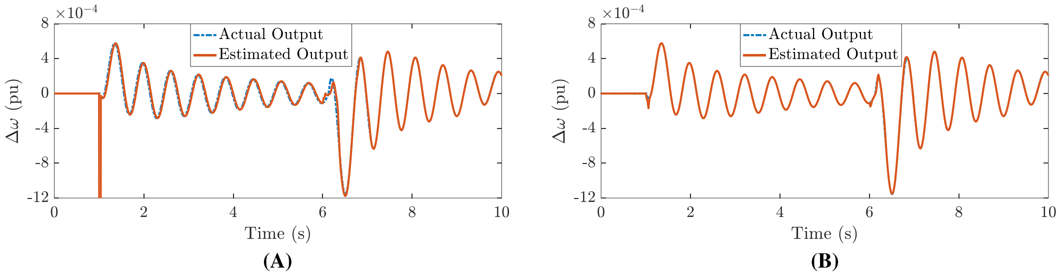

FIGURE 12 Identifier performance for SMIB in iteration number (A) 1 and (B) 2. [Colour figure can be viewed at wileyonlinelibrary.com]

TABLE 4 Comparison of neural-network architectural complexity.

Controller	Total layers	Total hidden neurons	Total connections	Type of neurons
Wang and MalikO[20]	4	20	144	Nonlinear
Farahani[21]	3	10	65	Nonlinear
Chang[22]	3	5	23	Nonlinear
Kamalasadan et al.[38]	3	15	270	Nonlinear
Kamalasadan and Swann[39]	3	15	270	Nonlinear
Al-Duwaish and Al-Hamouz[40]	3	30	124	Nonlinear
Farahani and Ganjefar[41]	4	8	37	Nonlinear
Farahani and Ganjefar[42]	3	10	65	Nonlinear
Tavakoli et al.[43]	4	8	37	
Tsai et al.[44]	3	9	70	Nonlinear
LNAC	*2*	*0*	*6*	*Linear*

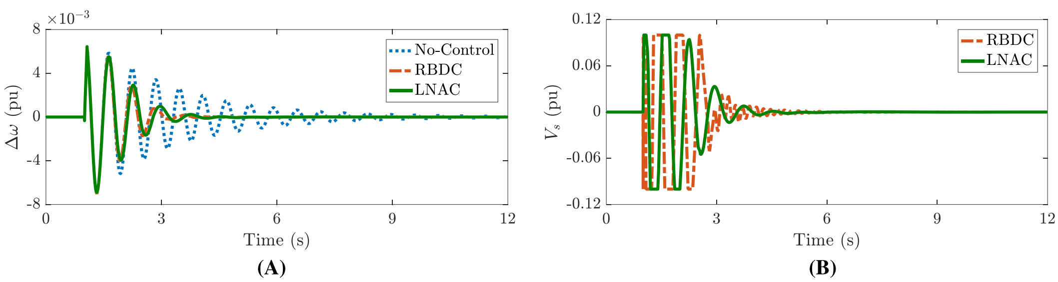

FIGURE 13 Performance of the SVC controller for nominal loading conditions ($P_G = 0.975$, $Q_G = 0.12$). [Colour figure can be viewed at wileyonlinelibrary.com]

In the existing literature, the use of a structurally complicated neural network with multiple layers and nonlinear neurons for power system identification has been continually employed, as, for example, given in Table 4. However, the proposed LNAC scheme, based on the simple neural identifier with only two layers and a linear neuron, faithfully approximates the local linear model of a power system. A non-linear identifier is generally used to model a complex system with stationary nonlinear dynamics and can be better utilized for off-line training. The performance of the identifier in the LNAC in the *second* iteration is also observed to be similar to the performance of the identification system implemented in Kamalasadan et al[38] in the *fiftieth* iteration, although the latter implementing a complex neural architecture.

The performance of the LNAC is now compared with that of the RBDC. Three-phase fault of four cycles at a frequency of 60 Hz was applied in the middle of the transmission line (in one circuit only). Figure 13 presents the plots of the generator's rotor speed deviation and the output of the controllers for four different operating conditions. It is clear from the plot in Figure 13A that both the LNAC and RBDC provide similar oscillation-damping performance at the nominal operating condition ($P_G = 0.975$, $Q_G = 0.12$). The stabilizing signal of both the controllers is also shown in Figure 13B where both the controllers are providing optimum control efforts to the system.

As the operating condition is altered to ($P_G = 1.5$, $Q_G = 0.37$), better performance of LNAC is observed as compared with RBDC (Figure 14A). It may be noted that the both the controllers were designed at the nominal operating conditions. Due to the overloading of the machine for operating condition II, the nonlinearities in the system manifest, thus affecting the oscillation damping. As the control signals are compared in Figure 14B, LNAC is seen to provide optimum control effort which results in its better oscillation-damping performance.

For operating conditions III ($P_G = 0.95, Q_G = -0.16$), the system controlled with RBDC becomes unstable with sustained oscillations, as shown in Figure 15A. The reason can be explained in Figure 15B where the control signal generated by RBDC is not stabilized thus affecting the system performance.

The fault duration was increased from four to six cycles for the loading condition IV ($P_G = 1.05, Q_G = -0.08$), and it is observed in Figure 16A that with RBDC, the system becomes unstable, whereas the LNAC controller is able to

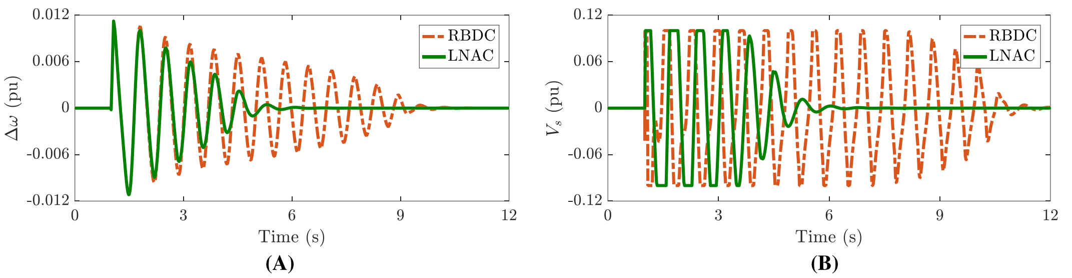

FIGURE 14 Performance of the SVC controller for loading condition II ($P_G = 1.5$, $Q_G = 0.37$). [Colour figure can be viewed at wileyonlinelibrary.com]

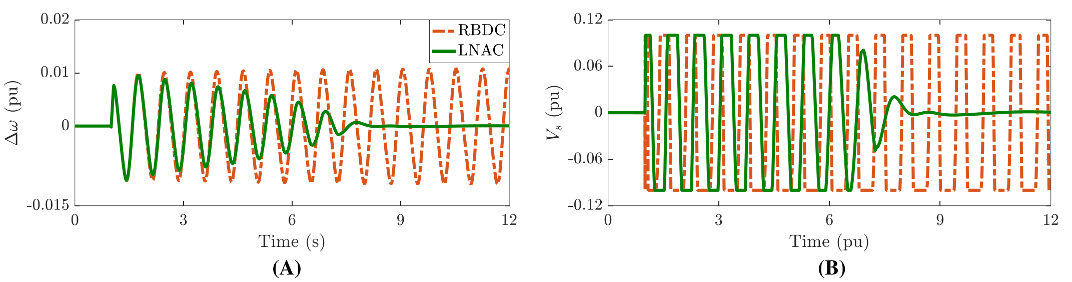

FIGURE 15 Performance of the SVC controller for loading condition III ($P_G = 0.95$, $Q_G = -0.16$). [Colour figure can be viewed at wileyonlinelibrary.com]

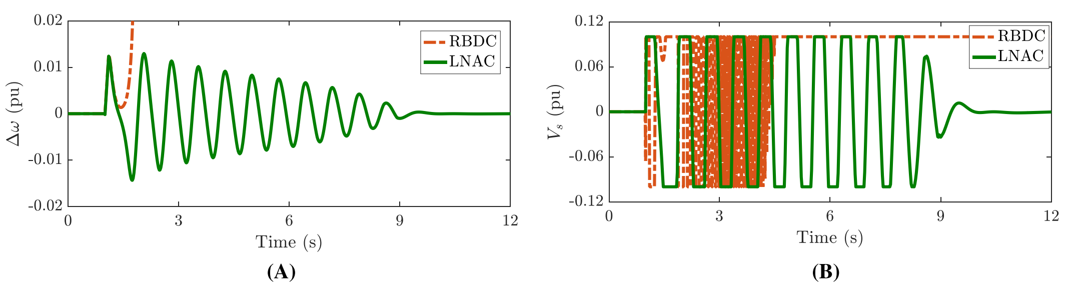

FIGURE 16 Performance of the SVC controller for loading condition III ($P_G = 1.05$, $Q_G = -0.08$). [Colour figure can be viewed at wileyonlinelibrary.com]

maintain stability and effectively damp out the oscillations. The plot of the control effort in Figure 16B shows the LNAC being able to provide stabilization to the system oscillations.

5.2 | Two-area four-machine power system

To evaluate the performance of damping controllers in multi-machine environment, an interconnected two-area power system each comprising of two machines with each machine having a rating of 900 MVA, as shown in Figure 17, is considered in this study.[13] This power system is a standard case of an inter-area mode with inadequate damping and this mode is observed in 220 km long tie-line which transfers 390 MW of active power from area 1 to area 2. PSSs are added in the generators G_1 and G_3 to damp local modes of oscillations. The loading conditions of the power system and parameters of the SVC (Base = 900 MVA) used are presented in Tables 5 and 6, respectively.

5.2.1 | Modal analysis

Using the mode shape and participation factors, critical oscillation modes are identified and tabulated in Table 7. It is observed that the inter-area mode has a nearly zero damping ratio, which may trigger system instability.

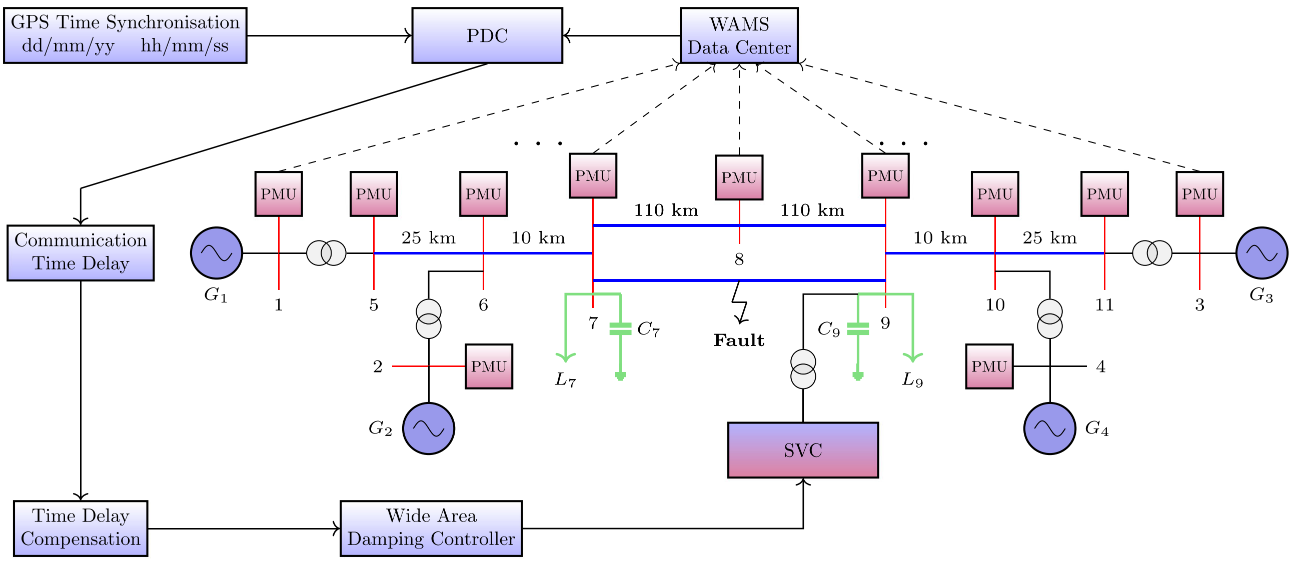

FIGURE 17 Configuration of two-area power system along with the components of WADC. [Colour figure can be viewed at wileyonlinelibrary.com]

TABLE 5 Loading conditions.

Nominal loading condition				**Altered loading condition**			
P_{7-8}		**405 MW**		P_{7-8}		**250 Mvar**	
P_{G_1}	700 MW	Q_{G_1}	185 Mvar	P_{G_1}	600 MW	Q_{G_1}	250 Mvar
P_{G_2}	700 MW	Q_{G_2}	235 Mvar	P_{G_2}	600 MW	Q_{G_2}	250 Mvar
P_{G_3}	722 MW	Q_{G_3}	185 Mvar	P_{G_3}	961 MW	Q_{G_3}	766 Mvar
P_{G_4}	700 MW	Q_{G_4}	202 Mvar	P_{G_4}	700 MW	Q_{G_4}	202 Mvar
P_{L_7}	967 MW	Q_{L_7}	−100 Mvar	P_{L_7}	967 MW	Q_{L_7}	−100 Mvar
P_{L_9}	1767 MW	Q_{L_9}	−250 Mvar	P_{L_9}	1767 MW	Q_{L_9}	−250 Mvar

TABLE 6 SVC parameters.

B_{ref}	0.025	T_v	0.15
B_{min}	−0.22	K_v	0.02
B_{max}	0.22	$V_{s_{min}}$	−0.1
X_t	0.08	$V_{s_{max}}$	0.1

TABLE 7 Modal analysis.

Eigenvalue	Type of mode	Freq. (Hz)	Damp. ratio (ζ)
$-0.003 \pm j3.7$	Inter-Area mode	0.6	0.0009
$-1.2 \pm j6.9$	Local mode 1	1.1	0.17
$-1.3 \pm j7.3$	Local mode 2	1.2	0.17

TABLE 8 Controllability and BVPF.

S.No	Bus number	
C_t	C_t rank	BVPF rank
1.	9	8
2.	5	9
3.	11	7
4.	7	6
5.	10	10
6.	6	5
7.	8	11

TABLE 9 Observability.

S.No.	Signal O_b rank	S.No.	Signal O_b rank
1.	ω_{1-3}	8.	δ_{2-3}
2.	δ_{1-3}	9.	ω_{2-3}
3.	P_{10-11}	10.	δ_{4-2}
4.	P_{7-8}	11.	ω_{4-2}
5.	ω_{1-4}	12.	Q_6
6.	δ_{1-4}	13.	Q_2
7.	P_{9-10}	14.	P_6

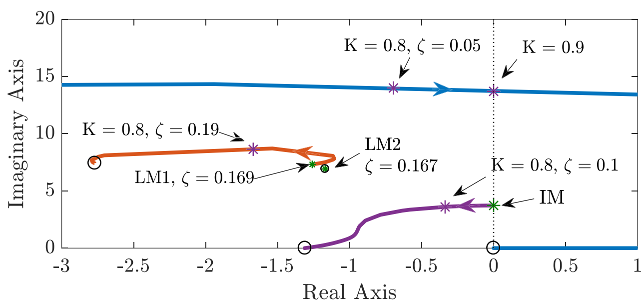

FIGURE 18 Root-locus plot at nominal operating condition. [Colour figure can be viewed at wileyonlinelibrary.com]

Table 8 shows the controllability order among various buses in the two-area power systems, corresponding to the inter-area oscillation mode and the BVPF order corresponding to the lowest eigenvalue (14.3) of J_R. The controllability order, as indicated in Table 8, favors bus 9 as the most suitable installation location for the SVC, and on the other hand, the BVPF order of the system favors bus 8. However, the controllability of bus 8 is the lowest among all the buses, which implies the low efficacy of SVC for damping control. Because of the priority of damping the undamped oscillation mode, a better trade-off for the SVC location would be bus 9. This choice is further supported by the fact that the

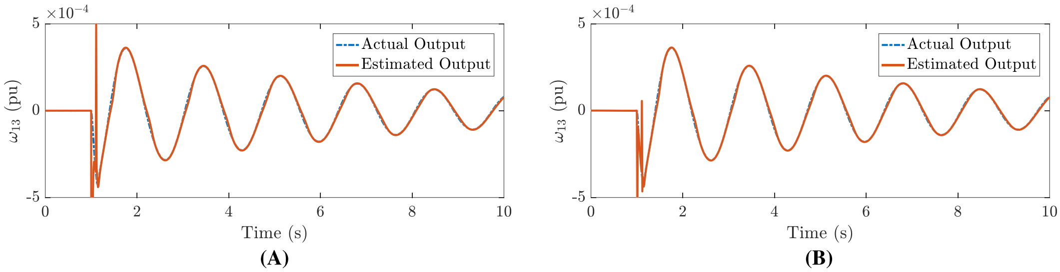

FIGURE 19 Neural identification of the system for (A) first iteration and (B) second iteration. [Colour figure can be viewed at wileyonlinelibrary.com]

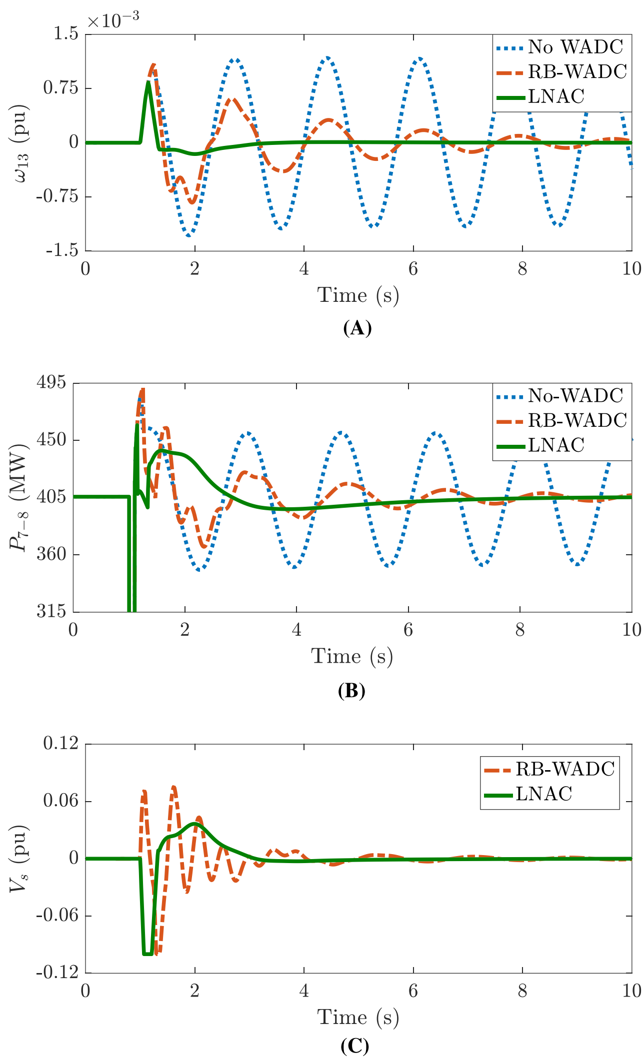

FIGURE 20 System's inter-area oscillation for nominal loading condition. [Colour figure can be viewed at wileyonlinelibrary.com]

lowest eigenvalue of J_R has a positive value, which indicates the voltage stability of the two-area power system. The observability of the power system measurements is used for the selection of feedback signal and their order is given in Table 9. The wide-area signal ω_{13} is observed to have the highest observability, which is consequently used as the feedback signal for the residue-based WADC (RB-WADC).

5.2.2 | Comparison between RB-WADC and LNAC

The values of T_1 and T_2 of the lead-lag controller for damping inter-area mode are obtained as 0.762 and 0.0945, respectively. In the root-locus plot shown in Figure 18, it is observed that with the increase in the value of K, the damping of the inter-area mode is improved whereas the damping ratio of the high-frequency mode is decreasing. Thus, the optimum value of K is selected as 0.8. At this value, the ζ of the high frequency mode and inter-area mode are 0.05 and 0.1, respectively.

For the LNAC, the penalty factor were adjusted as $\alpha = 1, \gamma = 0, \beta = 0$. The tracking performance of the system was validated by applying a 10% pulse disturbance to the V_{ref} of the SVC. Excellent tracking performance of the proposed linear identifier was observed as shown in Figure 19. The ISIE for the first few iterations is calculated as $(1.15, 0.098, 0.028, 0.012, 0.006) \times 10^{-7}$.

With the neural identifier being able to perfectly track the dynamics of two-area power system, the performance of the proposed LNAC and RB-WADC is now compared. A three-phase fault of four cycles was applied in the tie-line

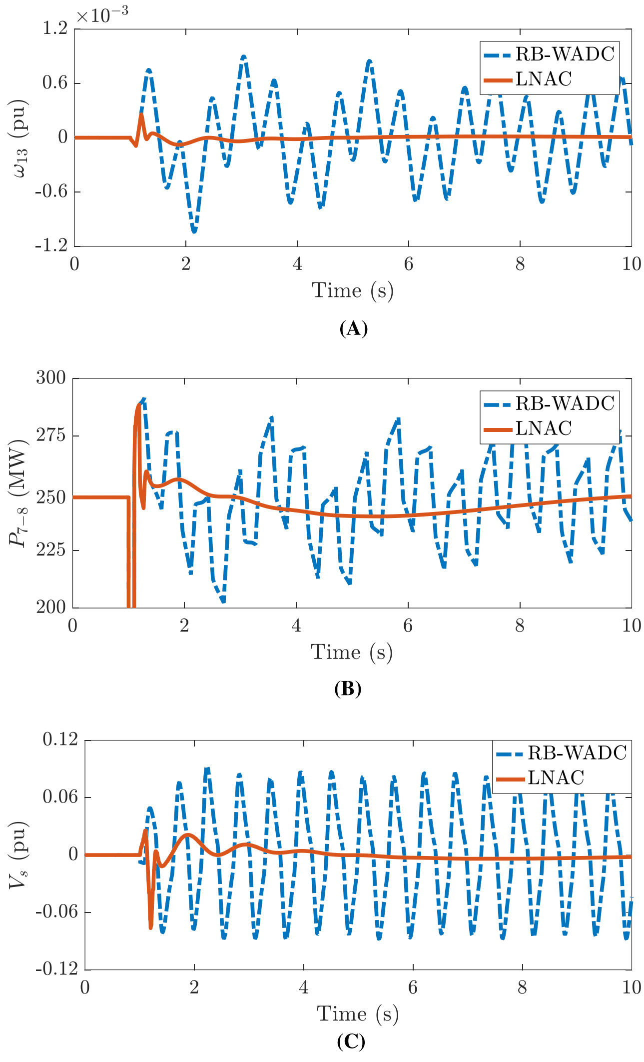

FIGURE 21 System's inter-area oscillation for altered loading condition. [Colour figure can be viewed at wileyonlinelibrary.com]

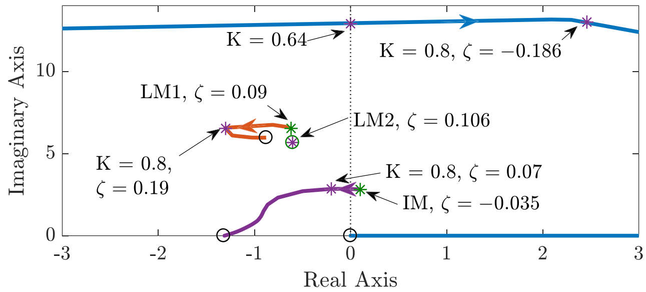

FIGURE 22 Root-locus at altered loading condition. [Colour figure can be viewed at wileyonlinelibrary.com]

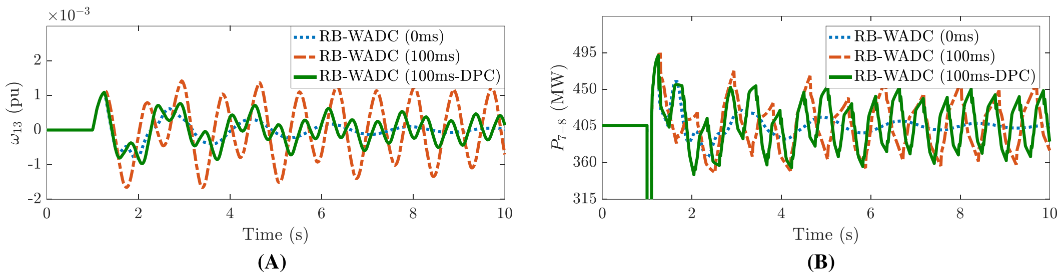

FIGURE 23 Inter-area oscillation for 0.1 s delay without and with DPC. [Colour figure can be viewed at wileyonlinelibrary.com]

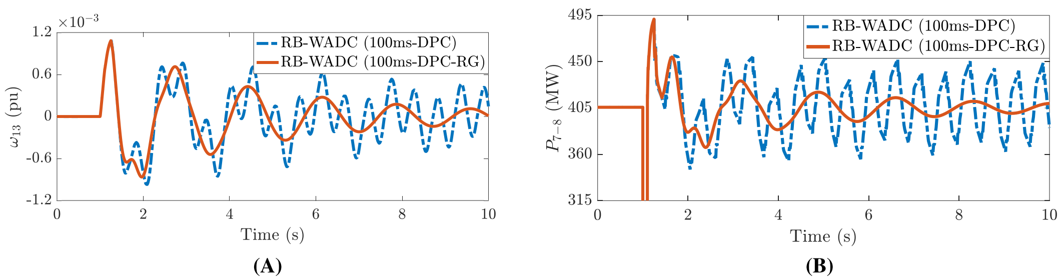

FIGURE 24 Inter-area oscillation with DPC without and with readjusted gain (RG). [Colour figure can be viewed at wileyonlinelibrary.com]

between the two areas as shown in Figure 17. It is observed from Figure 20A,B that the performance of LNAC in damping oscillations is significantly superior than that of the RB-WADC for the nominal loading condition given in Table 5. The superior damping is due to the optimum control effort of the adaptive controller as shown in Figure 20C. The installation of SVC also results in an increase of 15 MW of power over the tie-line.

For the altered loading condition given in Table 5, Figure 21A,B shows the performance of the RB-WADC, which has deteriorated and sustained oscillations are observed after the fault is cleared. However, with the LNAC, excellent oscillation damping is observed in the system. The output of the LNAC is also shown in Figure 21C. The deteriorated performance of RB-WADC for altered loading condition can also be explained in Figure 22. The designed values of the RB-WADC (nominal operating condition) when applied at altered loading condition shift the high-frequency mode in the unstable zone of the s-plane.

5.2.3 | Comparison between RB-WADC and LNAC incorporating delay

Communication delay was not included in the previous studies in transporting the signal ω_1 from area 1 and ω_3 from area 2 to the control center and then to the bus 9. The following investigations were conducted to asses the consequences of these communication delays on the controller's performance. The delay of 100 ms is introduced in the feedback signal, and the performance of both RB-WADC and LNAC is shown in Figure 23 for nominal loading condition. The deteriorated performance of the RB-WADC is obvious from the plots, which is due to the phase lag introduced in the signal due to the transportation time delay.

The DPC was added at the control input and its effect is also shown in Figure 23 where a substantial reduction in the magnitudes of oscillation peaks is observed. However, the damping of the system for the inter-area mode is still insufficient. After careful review of the system's frequency response, it is found that the higher frequency mode is located in the unstable region of the s-plane. This mode is introduced in the system due to delays and associated phase compensation.

TABLE 10 SVC gain required to damp high frequency mode.

Delay time (ms)	Phase lag (rad)	K	ζ of IA-mode
200	0.7442	0.32	0.05
400	1.4666	0.16	0.039
600	2.0968	0.09	0.031
800	2.5848	0.05	0.027
1000	2.9487	0.037	0.025

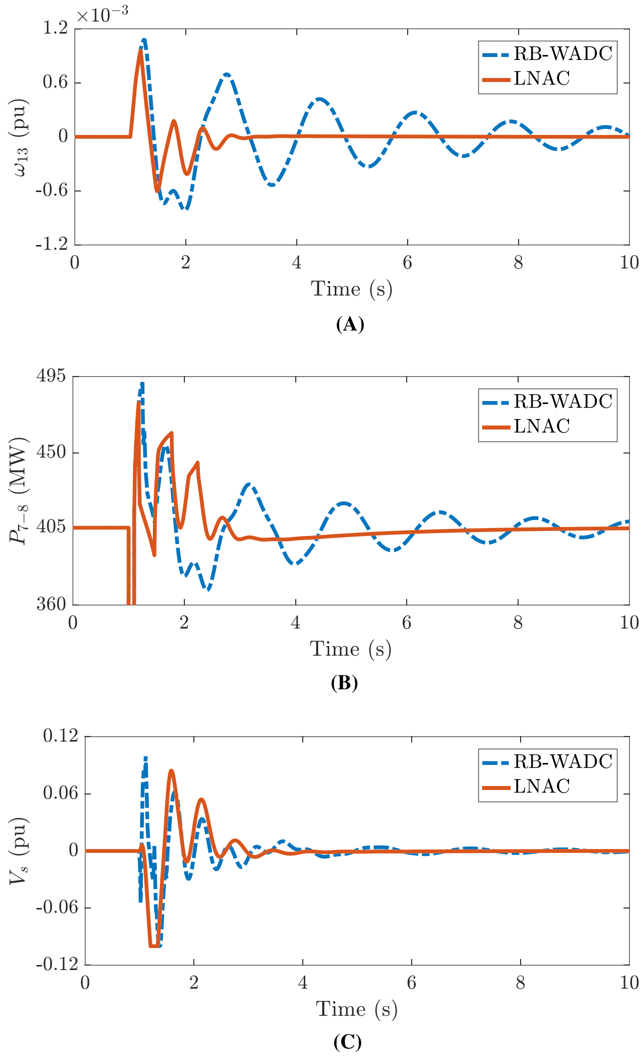

FIGURE 25 Comparison of controllers with 100 ms delay. [Colour figure can be viewed at wileyonlinelibrary.com]

Through the root locus plots, it is observed that as the gain of the RB-WADC is decreased from 0.8 to 0.56, the eigenvalue for the high-frequency mode is moved back to a stable region. The performance of RB-WADC with the revised controller gain setting is illustrated in Figure 24. Similarly, readjusted SVC gains for a wide range of time delays (0.1 to 1 s) were determined through root-locus plots and are displayed in Table 10. However, it is obvious from Table 10 that as the delay in the feedback signal is increased, the revised SVC gain is reduced, thus decreases the ζ of the inter-area mode and consequently deteriorating the performance of RB-WADC.

The performance of the LNAC at nominal loading condition for different values of communication delay is compared with the RB-WADC. The values of the SVC gain for the RB-WADC correspond to Table 10 and for the LNAC, no delay phase compensation is used. With the delay of 100 ms, both the controllers are able to damp the inter-area oscillation, however, the performance of the LNAC is seen to be much superior to that of the RB-WADC as shown in Figure 25A,B. The control effort by the LNAC and RB-WADC is also shown in Figure 25C, where better utilization of the SVC power by the LNAC is observed initially which subsequently leads to better oscillation damping as compared with the RB-WADC.

As the delay is increased to 350 ms, the performance of the RB-WADC is drastically deteriorated as shown in Figure 26A,B. In comparison, the LNAC is able to damp the oscillations in around 6 s only. The performance of RB-WADC is explained in Figure 26C, where the controller output is unable to generate an optimum control action and it oscillates between the maximum and minimum allowable value.

To check the efficacy of the LNAC, the delay is further increased to 800 ms and it is observed from the plots in Figure 27A,B that, in this case also LNAC is able to damp the oscillations, however, it takes around fifteen seconds to

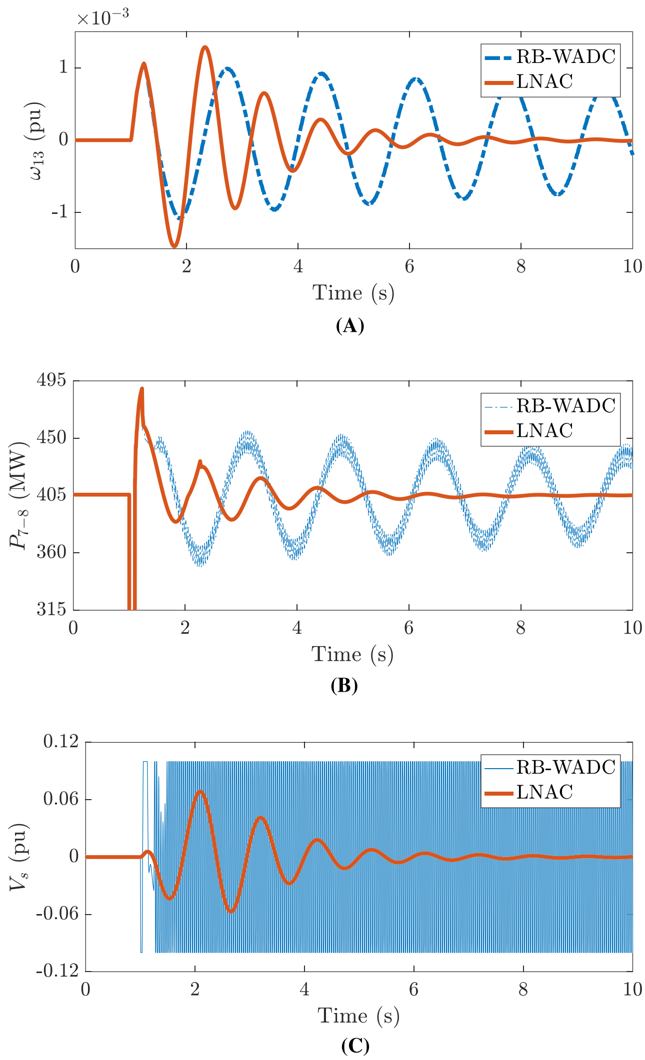

FIGURE 26 Comparison of controllers with 350 ms delay. [Colour figure can be viewed at wileyonlinelibrary.com]

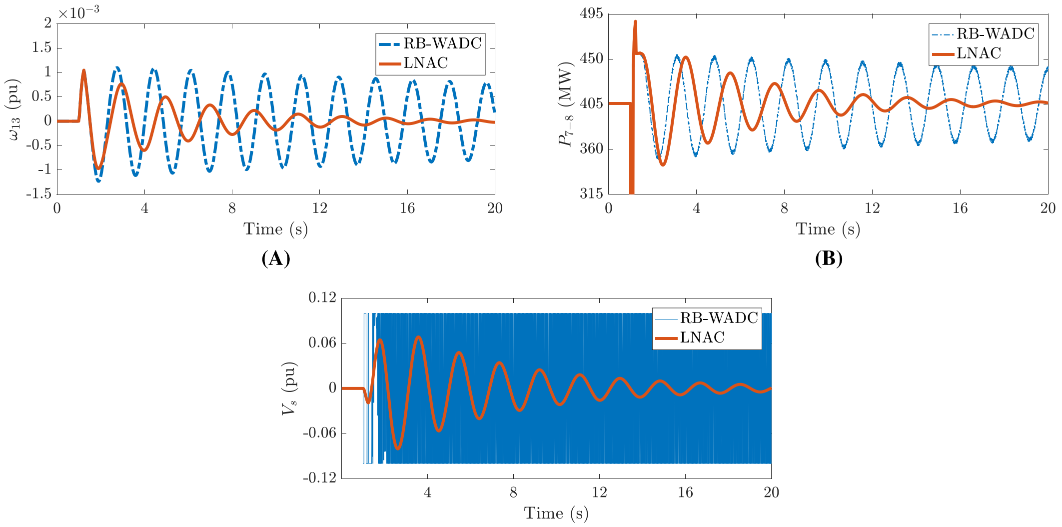

FIGURE 27 Comparison of controllers with 800 ms delay. [Colour figure can be viewed at wileyonlinelibrary.com]

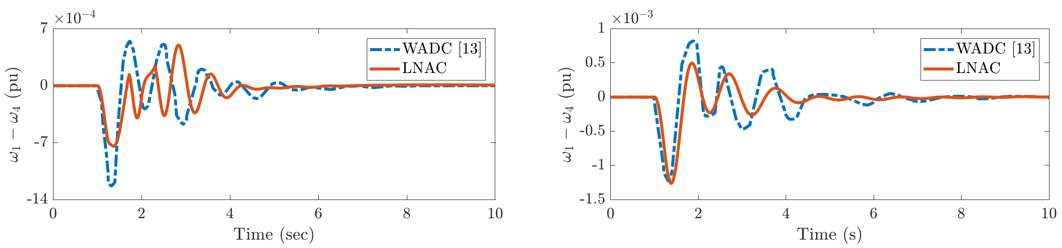

FIGURE 28 Comparison of WADC[13] with (A) 100 ms and (B) 300 ms delay. [Colour figure can be viewed at wileyonlinelibrary.com]

stabilize the system which is quite acceptable for such a high communication delay. The control action of the LNAC is also shown in Figure 27C.

5.2.4 | Comparsion between WADC[13] and LNAC

The performance of the LNAC was further compared with the WADC proposed in Yao et al.[13] This WADC[13] is designed using a residue method, and the Lyapunov stability criterion and linear matrix inequalities have been used for obtaining the delay margin and the gain of the controller. The designed controller is stable only up to 300 ms, and therefore, it is compared with LNAC for 100 ms and 300 ms. With the delay of 100 ms, both the controllers are able to damp the inter-area oscillation; however, the performance of the LNAC is slightly better than the RB-WADC as shown in Figure 28A. For the delay of 300 ms, the performance of the LNAC is far superior as compared with WADC[13] as shown in Figure 28B. The WADC[13] is unstable with delays more than 400 ms; however, the LNAC is stable with delays up to 800 ms as shown in Section 5.2.3.

6 | CONCLUSION

The residue-based damping controller is generally designed after linearizing the power system at a nominal loading condition. This controller, used as a supplementary controller for the static var compensator, may fail under varying loading conditions of the power systems. Moreover, the use of wide-area signals introduces time delays, which impede the efficiency of the controller. In this study, an empirical expression has also been proposed to offset the effects of communication time delays caused due to use of wide-area signals. But as the delay time is increased, the damping capability of the residue-based controller reduces quite significantly, even with delay compensation incorporated. Therefore, a neuro-adaptive control scheme has been proposed in this study, which has the additional advantage of being simple in architecture, thereby providing a minimal computational burden as compared with other existing neuro-controllers in the literature. It ensures swift control action and it is demonstrated that the proposed neural identifier is sufficient for online control schemes and that the use of complex network structures with nonlinear neurons is not required in such applications. Comprehensive simulation studies on nonlinear models of single-machine infinite-bus and two-area power systems were conducted, and the superior oscillation-damping performance of the proposed controller was demonstrated over various operating scenarios, time delays, and some previous studies.

In the optimal classification and regression decision tree (CART) can be integrated with the proposed neuro-adaptive controller to further limit the computational load of the controller for their application in oscillation damping.

CONFLICT OF INTEREST STATEMENT

The authors declare no conflict of interests.

DATA AVAILABILITY STATEMENT

Data sharing is not applicable to this article as no new data were created or analyzed in this study.

ORCID

Faisal Jamsheed https://orcid.org/0000-0002-3095-699X

REFERENCES

1. Wang G, Shen C, Fu L, Cui Z, Ye Z. Transformed periodic orbit mechanism of low frequency oscillations in power systems. *Int J Circuit Theory Appl*. 2016;44(1):226-239. doi:10.1002/cta.2073
2. Shahriar MS, Shafiullah M, Rana MJ, Ali A, Ahmed A, Rahman SM. Neurogenetic approach for real-time damping of low-frequency oscillations in electric networks. *Comput Electr Eng*. 2020;83:106600.
3. Kundur P, Canadian Electrical Association, Research and Development and Ontario Hydro and Ontario Hydro, and Analytical Methods and Specialized Studies Department. Investigation of low frequency inter area oscillation problems in large interconnected power systems. In: Research report (Canadian Electrical Association). Canadian Electrical Association; 1993.
4. Eremia M, Mihalic R, Blazic B. *Advanced Solutions in Power Systems*. Wiley-IEEE Press; 2016.
5. Salama HS, Vokony I. Voltage stability indices—a comparison and a review. *Comput Electr Eng*. 2022;98:107743.
6. Hasanvand H, Mozafari B, Arvan MR, Amraee T. Application of polynomial control to design a robust oscillation-damping controller in a multimachine power system. *ISA Trans*. 2015;59:343-353.
7. Al-Alawi SM, Ellithy KA. Tuning of svc damping controllers over a wide range of load models using an artificial neural network. *Int J Electr Power Energy Syst*. 2000;22(6):405-420.
8. Phadke AR, Fozdar M, Niazi KR. Robust tuning of fixed-parameter static var compensator controller for damping inter-area oscillations in power system. *Electr Pow Compo Syst*. 2010;38(8):974-995.
9. Baadji B, Bentarzi H, Bakdi A. Comprehensive learning bat algorithm for optimal coordinated tuning of power system stabilizers and static var compensator in power systems. *Eng Optim*. 2020;52(10):1761-1779.
10. Kumar R, Singh R, Ashfaq H. Stability enhancement of multi-machine power systems using ant colony optimization-based static synchronous compensator. *Comput Electr Eng*. 2020;83:106589.
11. Surinkaew T, Ngamroo I. Two-level coordinated controllers for robust inter-area oscillation damping considering impact of local latency. *IET Gener Transm Distrib*. 2017;11:4520-4530.
12. Kassem AM, Abdelaziz AY. Reactive power control for voltage stability of standalone hybrid wind–diesel power system based on functional model predictive control. *IET Renew Power Gener*. 2014;8(8):887-899. doi:10.1049/iet-rpg.2013.0199
13. Yao W, Jiang L, Wen J, Wu QH, Cheng S. Wide-area damping controller of facts devices for inter-area oscillations considering communication time delays. *IEEE Trans Power Syst*. 2014;29(1):318-329.
14. Yuan Y, Li G, Cheng L, Sun Y, Zhang J, Wang P. A phase compensator for svc supplementary control to eliminate time delay by wide area signal input. *Int J Electr Power Energy Syst*. 2010;32(3):163-169.
15. Nie Y, Zhang P, Cai G, Zhao Y, Xu M. Unified smith predictor compensation and optimal damping control for time-delay power system. *Int J Electr Power Energy Syst*. 2020;117:105670.
16. Fang DZ, Xiaodong Y, Chung TS, Wong KP. Adaptive fuzzy-logic SVC damping controller using strategy of oscillation energy descent. *IEEE Trans Power Syst*. 2004;19(3):1414-1421.
17. Wang S, Wang Z. Sliding mode dynamic surface control for multi-machine power systems with time delays and dead-zones. *Cybernet Syst*. 2021;52(1):58-72.

18. Bai J, Erlich I. A multi-objective model predictive controller for power oscillation damping and voltage control in power system. *IFAC-PapersOnLine*. 2018;51(28):398-403.
19. Lu C-F, Hsu C-H, Juang C-F. Coordinated control of flexible ac transmission system devices using an evolutionary fuzzy lead-lag controller with advanced continuous ant colony optimization. *IEEE Trans Power Syst*. 2013;28(1):385-392.
20. Wang H, Malik OP. Design of a neural network based SVC controller. *IFAC Proceedings Volumes*. 2005;38(1):64-69.
21. Farahani M. Intelligent control of SVC using wavelet neural network to enhance transient stability. *Eng Appl Artif Intell*. 2013;26(1): 273-280.
22. Chang Y-C. Robust neural network-based control of static var compensator. *IET Power Electron*. 2014;7(8):1964-1977.
23. Abdulrahman I, Radman G. Wide-area-based adaptive neuro-fuzzy SVC controller for damping interarea oscillations. *Can J Electr Comput Eng*. 2018;41(3):133-144.
24. Wang L, Truong D. Stability enhancement of a power system with a PMSG-based and a DFIG-based offshore wind farm using a SVC with an adaptive-network-based fuzzy inference system. *IEEE Trans Ind Electron*. 2013;60(7):2799-2807.
25. Zhang J, Wen JY, Cheng SJ, Ma J. A novel SVC allocation method for power system voltage stability enhancement by normal forms of diffeomorphism. *IEEE Trans Power Syst*. 2007;22(4):1819-1825.
26. Rogers G. *Power System Oscillations*. Boston, MA: Springer US; 2000.
27. Devi MM, Geethanjali M, Devi AR. Fault localization for transmission lines with optimal phasor measurement units. *Comput Electr Eng*. 2018;70:163-178.
28. T V, Jain T. Synchronized measurements-based wide-area static security assessment and classification of power systems using case based reasoning classifiers. *Comput Electr Eng*. 2018;68:513-525.
29. Shakarami MR, FarajiDavoudkhani I. Wide-area power system stabilizer design based on grey wolf optimization algorithm considering the time delay. *Electr Pow Syst Res*. 2016;133:149-159.
30. Philipp LD, Mahmood A, Philipp BL. An improved refinable rational approximation to the ideal time delay. *IEEE Trans Circuits Syst I: Fundam Theory Appl*. 1999;46(5):637-640.
31. Naghibi Z, Sadrossadat SA, Safari S. Adjoint recurrent neural network technique for nonlinear electronic component modeling. *Int J Circuit Theory Appl*. 2022;50(4):1119-1129. doi:10.1002/cta.3184
32. Noohi M, Mirvakili A, Sadrossadat SA. Modeling and implementation of nonlinear boost converter using local feedback deep recurrent neural network for voltage balancing in energy harvesting applications. *Int J Circuit Theory Appl*. 2021;49(12):4231-4247. doi:10.1002/cta.3143
33. Noohi M, Faraji A, Sadrossadat SA, Mirvakili A, Moftakharzadeh A. Modeling and implementation of a novel active voltage balancing circuit using deep recurrent neural network with dropout regularization. *Int J Circuit Theory Appl*. 2022. doi:10.1002/cta.3485
34. Ting NS, Aslay F, Sahin Y. A novel zero voltage transition boost converter and artificial neural network-based estimation of converter efficiency. *Int J Circuit Theory Appl*. 2022;50(9):3251-3265. doi:10.1002/cta.3337
35. Nørgaard M. *Neural Networks for Modelling and Control of Dynamic Systems: A Practitioner's Handbook*. Berlin New York: Springer; 2000.
36. Xia M, Antsaklis PJ, Gupta V, Zhu F. Passivity and dissipativity analysis of a system and its approximation. *IEEE Trans Autom Control*. 2017;62(2):620-635.
37. Anderson PM. *Power System Control and Stability*. Piscataway, N.J: IEEE Press Wiley-Interscience; 2003.
38. Kamalasadan S, Swann GD, Yousefian R. A novel system-centric intelligent adaptive control architecture for power system stabilizer based on adaptive neural networks. *IEEE Syst J*. 2014;8(4):1074-1085.
39. Kamalasadan S, Swann GD. A novel system-centric intelligent adaptive control architecture for damping interarea mode oscillations in power system. *IEEE Trans Ind Appl*. 2011;47(3).
40. Al-Duwaish HN, Al-Hamouz ZM. A neural network based adaptive sliding mode controller: application to a power system stabilizer. *Energy Convers Manage*. 2011;52(2):1533-1538.
41. Farahani M, Ganjefar S. An online trained fuzzy neural network controller to improve stability of power systems. *Neurocomputing*. 2015;162:245-255.
42. Farahani M, Ganjefar S. Intelligent power system stabilizer design using adaptive fuzzy sliding mode controller. *Neurocomputing*. 2017; 226:135-144.
43. Tavakoli AR, Seifi AR, Arefi MM. Designing a self-constructing fuzzy neural network controller for damping power system oscillations. *Fuzzy Sets and Systems*. 2019;356:63-76.
44. Tsai H, Liu J, Chu C. Integrations of neural networks and transient energy functions for designing supplementary damping control of UPFC. *IEEE Trans Ind Appl*. 2019;55:6438-6450.

How to cite this article: Jamsheed F, Javed Iqbal S. Intelligent wide-area damping controller for static var compensator considering communication delays. *Int J Circ Theor Appl*. 2023;1-29. doi:10.1002/cta.3560

APPENDIX

A | PROOF OF THEOREM 1

Proof. A positive semi-definite Lyapunov function is described and represented as

$$V(k)=\frac{1}{2}\boldsymbol{W_e}(k)\boldsymbol{W_e^T}(k) \tag{A1}$$

$$\boldsymbol{W_e}(k)=\boldsymbol{W}^{o}-\boldsymbol{W}^{I}(k). \tag{A2}$$

$\boldsymbol{W}^{o}$ is the value of the $\boldsymbol{W}^{I}(k)$ if the identifier output exactly matches the plant output. The change in Lyapunov function $\Delta V(k)$ can be expressed as

$$\Delta V(k)=\frac{1}{2}\Delta\boldsymbol{W_e}(k)\Delta\boldsymbol{W_e^T}(k)+\Delta\boldsymbol{W_e}(k)\boldsymbol{W_e^T}(k). \tag{A3}$$

Using (30) to (34) with (A) yields

$$\Delta\boldsymbol{W}^{I}(k-1)=\eta(k)\boldsymbol{I}(k-1)\boldsymbol{I}^{T}(k-1)\boldsymbol{W_e}(k-1). \tag{A4}$$

can be rewritten as

$$\Delta V(k)=-\Delta V_0(k)\left[2\eta(k)-\eta^2(k)\|\boldsymbol{I}(k-1)\|_2^2\right] \tag{A5}$$

$$\Delta V_0(k)=\frac{1}{2}\boldsymbol{W_e}(k)\boldsymbol{W_e^T}(k)\|\boldsymbol{I}(k-1)\|_2^2. \tag{A6}$$

With $\Delta V(k)<0$, system is asymptomatically stable. Using this property in (A5) results in

$$0<\eta(k)<\frac{2}{\|\boldsymbol{I}(k-1)\|_2^2}. \tag{A7}$$

■

To avoid division by zero, (A7) can be modified as

$$\eta(k)=\frac{\eta_o}{\|\boldsymbol{I}(k-1)\|_2^2+\epsilon} \tag{A8}$$

where $0<\eta_o<2$.

B | PASSIVE AND DISSIPATIVE SYSTEMS

Passive systems: A system is regarded to be a passive such that there exists a negative semi-definite function $V_1(x(k))$ and

$$<y,u>_{T_t}\geq V_1(x(k)) \tag{B1}$$

$$< y,u >_{T_t} = \sum_{k=1}^{T_t} y^T(k)u(k). \tag{B2}$$

Dissipative systems: A system is known to hold dissipativity of type $\boldsymbol{Q}$, $\boldsymbol{S}$, $\boldsymbol{R}$ such that supply rate $s(u,y)$ exists as a function of input(u) and output (y) and

$$s(u,y) \geq V_1(k) \tag{B3}$$

$$s(u,y) = < u,Ru >_{T_t} + 2 < y,Su >_{T_t} + < y,Qy >_{T_t}. \tag{B4}$$

where $\boldsymbol{Q}$, $\boldsymbol{S}$ and $\boldsymbol{R}$ being the constant matrices and $\boldsymbol{Q}$, $\boldsymbol{R}$ being the symmetric matrices. The system's dissipativity can be demonstrated using input-strict passivity with the following properties:

$$\boldsymbol{Q} = 0, \boldsymbol{R} = -\mu \boldsymbol{I}, \mu > 0, \boldsymbol{S} = 0.5\boldsymbol{I}. \tag{B5}$$

C | PROOF OF THEOREM 2

Proof. A negative semi-definite Lyapunov function is described and represented as

$$V_1(k) = -\frac{1}{2}\boldsymbol{W_e}(k)\boldsymbol{W_e}^T(k) \tag{C1}$$

$$\Delta V_1(k) = \Delta V_2(k) + \Delta V_3(k) \tag{C2}$$

$$\begin{aligned}\Delta V_2(k) = -\frac{1}{4}\Big[&\Delta \boldsymbol{W}^I(k)\Delta \boldsymbol{W}_I^T(k) - \Delta \boldsymbol{W}^I(k)\boldsymbol{W_e}^T(k) \\ &- \boldsymbol{W_e}(k)\Delta \boldsymbol{W}_I^T(k)\Big].\end{aligned} \tag{C3}$$

$$\Delta V_2(k) = [\boldsymbol{W_e}(k)]\left[\frac{\boldsymbol{I}}{2}\right][\Delta \boldsymbol{W}_I^T(k)] + [\Delta \boldsymbol{W}^I(k)]\left[\frac{-\boldsymbol{I}}{4}\right][\Delta \boldsymbol{W}_I^T(k)]. \tag{C4}$$

Using (A2) and (A4), $\Delta V_3(k)$ can be written as

$$\Delta V_3(k) = \Delta V_{3_0}(k)\left[2 - \eta(k)\|\boldsymbol{I}(k-1)\|_2^2\right] \tag{C5}$$

$$\Delta V_{3_0}(k) = \frac{1}{4}\eta(k)\boldsymbol{W_e}(k)\boldsymbol{W_e}^T(k)\|\boldsymbol{I}(k-1)\|_2^2 \tag{C6}$$

$$\begin{aligned}\Delta V_1(k) = \ &[\boldsymbol{W_e}(k)]\left[\frac{\boldsymbol{I}}{2}\right][\Delta \boldsymbol{W}_I^T(k)] + [\Delta \boldsymbol{W}^I(k)]\left[\frac{-\boldsymbol{I}}{4}\right][\Delta \boldsymbol{W}_I^T(k)] \\ &+ \Delta V_{3_0}(k)\left[2 - \eta(k)\|\boldsymbol{I}(k-1)\|_2^2\right].\end{aligned} \tag{C7}$$

A supply rate for the system in terms of (B4) can be expressed

$$
\begin{aligned}
s(k) = \ & [\boldsymbol{W_e}(k)][\mathbf{0}][\boldsymbol{W_e^T}(k)] + [\boldsymbol{W_e}(k)]\left[\frac{\boldsymbol{I}}{2}\right][\Delta \boldsymbol{W}_I^T(k)] \\
& + [\Delta \boldsymbol{W}^I(k)]\left[\frac{-\boldsymbol{I}}{4}\right][\Delta \boldsymbol{W}_I^T(k)].
\end{aligned} \tag{C8}
$$

With $\boldsymbol{Q} = \boldsymbol{0}, \boldsymbol{R} = -0.25\boldsymbol{I}, \boldsymbol{S} = 0.5\boldsymbol{I}$, in (B4), input-strictly passivity is proved if (40) is satisfied, which follows

$$
s(k) \geq V_1(k) \tag{C29}
$$

and, hence, the system's dissipativity is inferred. ■